Dalton Transactions

ROYAL SOCIETY OF CHEMISTRY

PAPER

View Article Online
View Journal



Cite this: DOI: 10.1039/d6dt00206d

# Water-soluble silver nanoparticles stabilized by amino acid-derived N-heterocyclic carbenes: synthesis, properties and theoretical study of the nucleation process

Carlos J. Carrasco, [a] Regla Ayala, [a,b] Sara Garrido,[a] Francisco Montilla *[a] and Agustín Galindo [a]

Silver nanoparticles stabilized by amino acid-derived N-heterocyclic carbenes, denoted as Ag(NHC$^{R}$)-NPs (R = H, **3a**; Me, **3b**; $^{i}$Pr, **3c**; and $^{i}$Bu, **3d**), were synthesized by reducing the parent complexes $Na_3$[Ag(NHC$^{R}$)$_2$] (**2a–d**) with $NaBH_4$ under appropriate reaction conditions. The stability of the aqueous AgNP solutions was found to depend strongly on the presence of the NHC ligand, the solution concentration, and the nature of the R substituent. In particular, the stability of the nanoparticles decreases as the steric bulk of R increases. Among the series, **3a** (R = H) exhibits remarkable stability in water and can be isolated by ultracentrifugation and lyophilization. Notably, solid Ag(NHC$^{H}$)-NPs (**3a**) can be redissolved in water to regenerate a stable AgNP solution. The Ag(NHC$^{R}$)-NPs were characterized by infrared (IR) and ultraviolet-visible (UV-Vis) spectroscopies, polarimetry, dynamic light scattering (DLS), and transmission electron microscopy (TEM). **3a** behaves as an active and versatile nanocatalyst in water, efficiently promoting both the model reduction of 4-nitrophenol to 4-aminophenol and the catalytic hydrolysis of $NaBH_4$ to generate $H_2$ under basic conditions. From a theoretical perspective, the nucleation and growth of the Ag(NHC$^{R}$)-NPs were modelled using density functional theory (DFT) at the PBE-D3/def2-TZVP level, considering systems of the type $[Ag_n(NHC^{R})]^{2-}$ (with R = H, Me and $^{i}$Pr and $n$ = 2, 3, 4, 20, 30). The Quantum Theory of Atoms in Molecules (QTAIM) was employed to analyze the bonding characteristics within the nanoparticles, with particular attention to the Ag–Ag and Ag–C(carbene) interactions. It is noteworthy that the bond dissociation energy (BDE) of the Ag–C(carbene) bond decreases with increasing steric bulk of R, consistent with the experimental observations. Based on experimental data, the Ag : NHC ratio is approximately 30 : 1 and the calculated IR spectrum of $[Ag_{30}(NHC^{H})]^{2-}$ model (corresponding to **3a**) provides a satisfactory match with the experimental spectrum.

Received 26th January 2026,
Accepted 1st March 2026

DOI: 10.1039/d6dt00206d

rsc.li/dalton



## Introduction

Silver nanoparticles (AgNPs) have garnered significant attention because of their unique physicochemical properties—such as high surface area, tuneable optical characteristics, and strong antimicrobial activity—which have enabled their application in various fields, including catalysis, electronics, medicine, and environmental remediation. Among the various synthetic strategies, biological and ligand-assisted methods have gained prominence for producing stable, functionalized nanoparticles under mild conditions. In particular, the use of organic ligands has proven effective in enhancing colloidal stability, controlling particle size, and adjusting surface reactivity.[1–5] In this context, N-heterocyclic carbenes (NHCs) have emerged as a versatile class of ligands for nanoparticle stabilization. Their strong $\sigma$-donor character facilitates the formation of robust metal–ligand bonds, imparting resistance to aggregation and oxidative degradation.[6–8] The structural tunability of NHCs—*via* modifications of the heterocyclic core, substituents, and side chains—enables precise control over the steric and electronic properties, making them ideal for surface functionalization. Recent reviews underscore their growing role in materials chemistry, particularly in stabilizing metal nanoparticles for catalytic applications.[4–7] Despite these advances, aqueous solubility remains a key challenge for NHC-stabilized nanoparticles, particularly in biomedical contexts.[9,10] To address this, recent efforts have focused on incorporating hydrophilic functional groups into the NHC framework.[11,12]

In recent years, our research has focused on the development of amino acid-derived imidazolium carboxylates as pre-

[a]*Departamento de Química Inorgánica, Facultad de Química, Universidad de Sevilla, 41012 Sevilla, Spain*
[b]*Instituto de Ciencia de Materiales de Sevilla-CSIC. Avda. Américo Vespucio 49, 41092 Sevilla, Spain. E-mail: montilla@us.es*

cursors for silver–N-heterocyclic carbene complexes (Ag–NHC). This interest led us to investigate the different biomedical properties of these compounds. Amino acid-derived NHC ligands present a promising approach by integrating the stabilizing characteristics of carbenes with the inherent water solubility and biocompatibility of amino acid moieties.[13–16] Moreover, these ligands can improve the colloidal stability of silver nanoparticles through steric hindrance and hydrogen bonding, while simultaneously introducing functional groups capable of promoting interactions with biological systems. Leveraging the synthetic versatility of NHCs and the inherent biocompatibility of amino acid residues, we aim to develop a new class of AgNPs suitable for aqueous environments.

Density functional theory (DFT) has emerged as a powerful tool to investigate the structure, properties and reactivity of silver clusters,[17–21] particularly those stabilized by selected ligands.[4,22–24] Beyond providing optimized geometries and electronic structures for NHC-stabilized nanoparticles, DFT can identify the preferred ligand coordination sites, the role of NHC in stabilizing larger clusters, and the energetics underlying nanoparticle growth. Such theoretical insights complement and validate experimental observations, offering a molecular-level framework that is essential for understanding and ultimately controlling the properties of silver-based nanomaterials. In addition, the Quantum Theory of Atoms in Molecules (QTAIM[25–30]) was employed to characterize the nature and presence of bonding as well as the degree of covalence and interaction strength between the silver nanoparticles (AgNPs) and the carbene functionality.

In this study, we report on the synthesis, characterization and theoretical study of AgNPs stabilized by amino acid-derived NHCs, focusing on their solubility, structural integrity, potential applications, and DFT analysis of the silver–silver bond and NP nucleation and growth. As a preliminary demonstration of their catalytic potential, the nanoparticles were evaluated in the aqueous-phase reduction of 4-nitrophenol with $NaBH_4$ and in the hydrolysis of $NaBH_4$ to evolve $H_2$ under basic conditions, both being benchmark reactions widely employed to evaluate the catalytic activity of noble metal nanoparticles.[31–33]

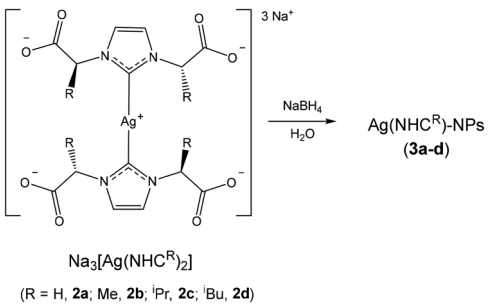


$Na_3[Ag(NHC^R)_2]$

(R = H, **2a**; Me, **2b**; $^i$Pr, **2c**; $^i$Bu, **2d**)

**Scheme 1** Silver nanoparticles stabilized by N-heterocyclic carbene.

**Table 1** Stability of Ag(NHC$^H$)-NP (**3a**) *versus* non-stabilized AgNPs at different concentrations

| | Time of decomposition | |
|---|---|---|
| Concentration | Ag(NHC$^H$)-NP (**3a**) | Non-stabilized AgNPs |
| 1 mM | — | 20 h |
| 2 mM | 48 h | 2 h |
| 5 mM | 20 h | 2 h |
| 10 mM | 2 h | 2 h |

# Results and discussion

### Nanoparticles from Ag–NHC complexes

Silver nanoparticles stabilized with N-heterocyclic carbene ligands, Ag(NHC$^R$)-NPs (R = H, **3a**; Me, **3b**; $^i$Pr, **3c**; and $^i$Bu, **3d**), were synthesized *via* a bottom-up approach. This involved the reduction of previously reported silver complexes, $Na_3[Ag(NHC^R)_2]$ (**2a–d**),[15,16] with $NaBH_4$ in aqueous solution (Scheme 1). To optimize the synthesis procedure, Ag(NHC$^H$)-NPs (**3a**) were initially prepared at concentrations of 1 mM, 2 mM, 5 mM, and 10 mM, using $Na_3[Ag(NHC^H)_2]$ (**2a**) as the precursor. The stability of the resulting nanoparticles was assessed using UV-visible spectroscopy by monitoring the localized surface plasmon resonance (LSPR) band centred around 400 nm (Table 1).[34]

Notably, the nanoparticles synthesized at the highest concentration (10 mM) exhibited rapid decomposition, characterized by the loss of the yellow coloration of the solution, the formation of precipitated agglomerated silver particles and the disappearance of the LSPR band in two hours. Synthesized at lower concentrations, 5 mM and 2 mM, demonstrated improved stability, although they also underwent decomposition within 20 and 48-hours after synthesis, respectively. Nanoparticles synthesized at the lowest concentration (1 mM) showed the greatest stability, remaining stable for several months (stored in the dark at room temperature). The initially observed LSPR band decreases during the first hour after nanoparticle dispersion in suspension, likely due to aggregation phenomena. However, from the second hour onwards, the band intensity remains virtually unchanged, persisting even three months after nanoparticle formation (Fig. 1).

To assess the size distribution of Ag(NHC$^H$)-NPs (**3a**), dynamic light scattering (DLS) measurements were conducted on a 1 mM colloidal solution (Fig. S1). The analysis indicated a narrow size distribution with low polydispersity and an average particle diameter below 10 nm. These results were further validated by transmission electron microscopy (TEM). Image analysis of the TEM micrographs using ImageJ software revealed an average nanoparticle diameter of 8.2 ± 2.2 nm (SD) (Fig. S2), in good agreement with the principal peak observed in the DLS data.

In addition, Ag(NHC$^H$)-NPs (**3a**) were isolated by ultracentrifugation followed by lyophilization. The isolated nanoparticles can be redispersed in water, retaining key properties observed

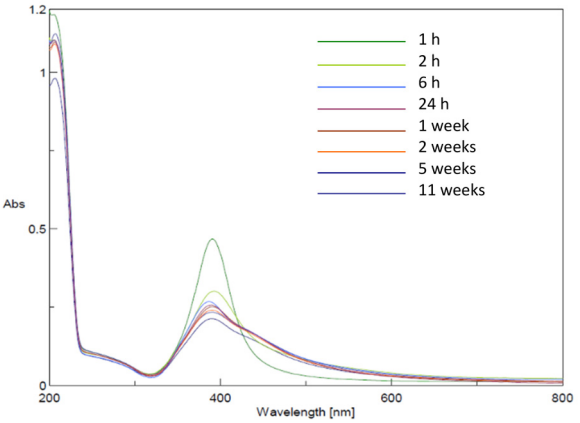


**Fig. 1** UV-vis spectrum of Ag(NHC$^{H}$)-NPs (**3a**) over time.

prior to isolation, such as the intensity of the LSPR band. The ATR-IR spectrum of isolated nanoparticles displays characteristic absorption bands attributable to the imidazole-carboxylate moiety, indicating its coordination to silver atoms on the nanoparticle surface. For **3a**, two distinct bands at 1627 and 1571 $cm^{-1}$ were assigned to the asymmetric stretching vibrations of the two carboxylate ($COO^{-}$) groups (Fig. S3). Additionally, absorptions at 1381 and 1313 $cm^{-1}$ were attributed to the symmetric $\nu(COO^{-})$ of the carboxylate groups. These assignments were confirmed by theoretical data (see below) and attributed to the NHC ligand. Furthermore, CHN elemental analysis revealed an approximate ratio of one carbene ligand per 30 silver atoms within the nanoparticle structure.

To verify the stabilizing effect of NHC ligands on silver nanoparticles, non-stabilized AgNPs were also synthesized using a procedure analogous to that described for the synthesis of **3a**, but with $AgNO_3$ as the precursor (Table 1). In all cases, the stability of these nanoparticles was significantly lower than that of **3a**, particularly at concentrations of 2 mM, 5 mM, and 10 mM, where complete decomposition occurred within 2 hours. At a lower concentration of 1 mM, the non-stabilized nanoparticles exhibited slightly greater stability, yet they still decomposed within approximately 20 hours. Moreover, DLS analysis reveals a higher polydispersity of AgNPs (Fig. S4), indicating the presence of two predominant nanoparticle sizes, approximately 2.7 and 8.7 nm.

To investigate the influence of the ligand on the synthesis of the nanoparticle, the preparation of AgNPs **3b–d** was investigated. They were prepared by reduction of the precursors $Na_3[Ag(NHC^{R})_2]$ (R = Me, **2b**; $^{i}$Pr, **2c**; $^{i}$Bu, **2d**) at 1 mM concentration, under the experimental conditions optimized for **3a**. The chiral nature of AgNPs was maintained after reduction as proved by polarimetry measurements (for example, $\alpha_D^{25}$ of 24.0° ± 0.2 for **3c** in water). The stability of the nanoparticles was initially assessed by monitoring the intensity of the LSPR band over time. As observed for nanoparticles **3a**, a decrease in band intensity was also detected during the first hour following the formation of **3b–d**, which is likely attributable to initial aggregation processes. After this initial period, the nanoparticles remained stable for several weeks (Fig. S5). DLS and TEM analyses of **3c** nanoparticles confirmed a uniform composition, with an average particle size of approximately 10 nm (Fig. S6). Comparable morphologies and size distribution were observed in TEM analyses of nanoparticles **3b** and **3d** (Fig. S7).

### Catalytic activity of AgNPs in the reduction of 4-nitrophenol and the hydrolysis of $NaBH_4$

To explore the catalytic potential of these AgNPs, we investigated the performance of **3a** in aqueous media, where it efficiently facilitates both the model reduction of 4-nitrophenol (4-NP) to 4-aminophenol (4-AP) and the catalytic hydrolysis of $NaBH_4$ for dihydrogen generation under basic conditions. The development of efficient nanocatalysts for environmentally relevant redox processes represents a key challenge in sustainable chemistry, particularly for wastewater remediation and on-demand hydrogen generation.[35] The reduction of 4-NP using $NaBH_4$ serves as a benchmark reaction for noble metal nanoparticles, given the toxicity of nitroaromatic pollutants from industrial effluents and the pharmaceutical value of the amino product.[36] Similarly, the catalytic hydrolysis of $NaBH_4$ constitutes a promising route for portable $H_2$ production, offering high-purity gas from a stable solid-state hydrogen carrier suitable for fuel cells.[33] In the presence of excess $NaBH_4$ (1 : 10 4-NP : $NaBH_4$), **3a** mediates a clean transformation of 4-NP into 4-AP, as evidenced by the gradual decay of the 400 nm band of 4-NP and the concomitant growth of the 4-AP band at shorter wavelength (Fig. S8). As illustrated in Fig. 2, the reaction follows an apparent pseudo-first-order kinetic model with respect to 4-NP, with an approximately linear dependence of $\ln(C/C_0)$ on time over the main conversion interval and a rate constant $k$ = 0.16 $min^{-1}$, consistent with a surface-mediated electron-transfer process from borohydride to 4-NP on the Ag–NHC nanoparticles. The steady decrease of the 4-NP absorbance from high initial values to near-plateau after several minutes, without induction periods or evidence of deactivation, reflects both the intrinsic activity of **3a** and its colloidal robustness in water. These features place **3a** in line with other NHC-stabilized AgNP systems

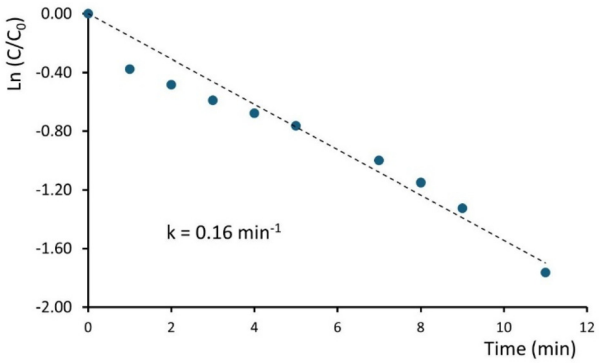


**Fig. 2** Catalytic activity of Ag(NHC$^{H}$)-NPs (**3a**) in the reduction of 4-NP.

reported as benchmarks for 4-NP reduction, for example $k \approx 0.5\ min^{-1}$ for related systems,[22] where high-rate constants are associated with small particle sizes and partially accessible metal surfaces. The same nanoparticle system also catalyses hydrogen evolution from $NaBH_4$ in basic aqueous medium, demonstrating that **3a** can efficiently activate borohydride beyond its role as a simple reducing agent. When 1 mmol of $NaBH_4$ is treated with 0.05 mmol of the Ag–NHC precursor **2a** (forming **3a** *in situ*), significant $H_2$ production is observed at pH ≈ 11.5, reaching about 50 mL of gas under conditions where uncatalyzed or purely basic media give negligible or very slow evolution (Fig. S9). A direct comparison with AgNPs generated from $AgNO_3$ under the same basic conditions shows that the NHC-stabilized system clearly outperforms the non-stabilized particles, which produce only around 35 mL of $H_2$ from the same $NaBH_4$ charge. This difference, together with the known higher colloidal stability and narrower size distribution of **3a**, indicates that NHC capping improves not only nanoparticle lifetime but also the effective density of active sites available for borohydride activation. Combining both sets of results, **3a** emerges as a robust Ag-based nanocatalyst capable of promoting two mechanistically related but distinct redox processes in water: the reduction of an aromatic nitro group and the hydrolytic decomposition of borohydride. In both cases, the catalytic performance of **3a** can be rationalized by considering its structural features. The nanoparticles exhibit a small average diameter in the sub-10 nm range and a low NHC-to-Ag ratio, which ensures a high density of accessible metallic surface sites while maintaining excellent colloidal stability in water. This balance between stabilization and surface exposure prevents extensive aggregation or deactivation during the reduction, in contrast to non-stabilized AgNPs that usually display shorter lifetimes and poorer kinetic profiles. The absence of a pronounced induction period also suggests that the active surface of **3a** is readily available to both 4-nitrophenol and borohydride from the onset of the reaction.

## Theoretical calculations

To obtain information on the interaction of NHC ligands and silver nanoparticles, it was considered worthwhile to initiate the study with the simplest systems: one to four silver atoms. Initially, the coordination of the ligands $(NHC^R)^{2-}$ ($NHC^R$ for R = H, Me and $^i$Pr) to a single silver(0) atom was analyzed using density functional theory (DFT). Geometry optimizations of $[Ag(NHC^R)]^{2-}$ were performed without symmetry restrictions and their optimized structures are shown in Fig. 3. We previously studied the interaction of these ligands with silver(I) ions in complexes $[Ag(NHC^R)_2]^{3-}$ and the frontier molecular orbitals (MOs) of ligands $(NHC^R)^{2-}$ were well identified.[14,16] Comparison of the interaction between $NHC^R$ and silver(0) with respect to that with silver(I) is pertinent to evaluate whether coordination capabilities are maintained similarly. Therefore, geometry optimizations of $[Ag(NHC^R)]^-$ were also carried out and the resulting optimized structures are shown in Fig. S10. As expected, the Ag–C distances (range 2.161–2.164 Å) in the silver(0) species are longer than those

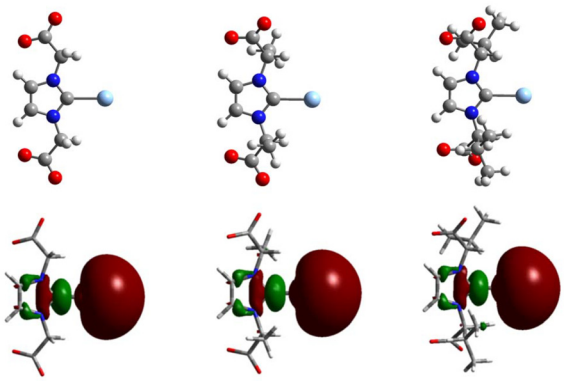

**Fig. 3** Optimized structures (top) and SOMOs (bottom) of $[Ag(NHC^R)]^{2-}$ for R = H, Me and $^i$Pr.

found for the silver(I) compounds. The calculated bond dissociation energies (BDEs) for the Ag–C bond of $[Ag(NHC^R)]^{2-}$ are around 31 kcal $mol^{-1}$ (Table S1). These BDE values are lower than the values found for NHC silver complexes with the acetate ligand (around 68 kcal $mol^{-1}$, Table S1). The SOMO of $[Ag(NHC^R)]^{2-}$ species is a non-bonding MO centered on the silver atom (composition for R = H: 55% s orbital and 29% p orbital) with a small antibonding combination with the carbon atom of NHC (Fig. 3) that justifies the reduction in the length of the Ag–C bond. This fits well with the simplified MO diagram shown in Fig. S11, where the Ag–C bond is mainly located in SOMO−8. Selected local and integral topological properties of the electron density for silver(I) and silver(0) complexes are presented in Table 2. Specifically, the electron density ($\rho_{BCP}$) and its Laplacian($\nabla^2\rho_{BCP}$) were used as preliminary indicators of the presence and nature of bonding, where negative and positive values for the Laplacian of the electron density at the bond critical point (BCP) are assigned to electron-shared and closed-shell interactions, respectively.[25] However, it is well-known that this assignment is inefficient for the description of heavy atoms interactions.[37] In this context, Macchi's classification[38–40] was also adopted, based on a combination of local and integral properties within atomic basins. Key metrics utilized included the delocalization index, $\delta(A,B)$, which reveals the extent of electron pair exchange (bonding mechanism), and the integrated electron density, $\int A \cap B$, which is indicative of the interaction strength. Furthermore, the bonding regime was quantitatively assessed using the energetic ratio of the potential energy density to the kinetic energy density at the BCP, ($|V_{BCP}|/G_{BCP}$). Values of $|V_{BCP}|/G_{BCP} < 1$ were assigned to ionic/van der Waals interactions, while values > 2 indicated covalent interactions, with the intermediate range ($1 < |V_{BCP}|/G_{BCP} < 2$) characterizing dative bonds or ionic bonds with weak covalent character. The degree of covalence was additionally estimated from the ratio of the total energy density to the electron density $H_{BCP}/\rho_{BCP}$ (being $H(r) = [G(r) + V(r)]$),[37] and the interaction strength was quantified using the Espinosa *et al.* correlation scheme, $E_{int} = -1/2V_{BCP}$.[41–43] The analysis of these topological properties

**Table 2** Selected local and integrated topological properties of the electron density at the Ag–X (X being C, O and H) for $[Ag(NHC^R)]^{n-}$ ($n$ = 1, 2) complexes[a]

| Complex | Ag–X | $Dist_{(Ag-X)}$ | $\rho$ | $\nabla^2\rho$ | $\delta$(Ag,X) | $\int_{Ag\cap X}\rho$ | $\lvert V\rvert/G$ | $H/\rho$ | $E_{int}$ |
|---|---|---|---|---|---|---|---|---|---|
| $[Ag(NHC^H)]^-$ | C | 2.051 | 0.114 | 0.256 | 0.951 | 0.952 | 1.389 | −0.357 | −45.613 |
| $[Ag(NHC^H)]^{2-}$ | C | 2.161 | 0.091 | 0.253 | 0.826 | 0.824 | 1.276 | −0.264 | −34.798 |
| $[Ag(NHC^{Me})]^-$ | C | 2.048 | 0.115 | 0.257 | 0.953 | 0.971 | 1.391 | −0.360 | −46.120 |
| $[Ag(NHC^{Me})]^{2-}$ | C | 2.161 | 0.091 | 0.252 | 0.814 | 0.864 | 1.277 | −0.264 | −34.798 |
| $[Ag(NHC^{iPr})]^-$ | C | 2.099 | 0.102 | 0.261 | 0.825 | 0.895 | 1.329 | −0.314 | −40.655 |
| $[Ag(NHC^{iPr})]^{2-}$ | C | 2.164 | 0.091 | 0.253 | 0.798 | 0.860 | 1.273 | −0.262 | −34.844 |

[a] All dimensions are expressed in atomic units (a.u.) except distances which are in Å and $E_{int}$, which is in kcal mol$^{-1}$. $\delta$(Ag,X) means the delocalization index between Ag–X bonded atoms. $\int_{Ag\cap X}\rho$ accounts for the integrated electron density on the whole Ag–X interatomic surface. $\lvert V\rvert/G$ is an adimensional ratio at the BCP and $H/\rho$ is the total energy ratio at the BCP.

reinforces previous conclusions, that is, more stability of the silver(I) species respect to the silver(0). This is evident from the larger values of $\rho_{BCP}$, $\nabla^2\rho_{BCP}$, $\delta$(Ag,C), $\int_{Ag\cap C}\rho$ and estimated $E_{int}$ energies for the former compared to the silver(0) species (Table 2). The possible interaction of $(NHC^R)^{2-}$ ligands through the oxygen atom of carboxylate with the silver(0) atom was also analyzed, but the energies of the $[Ag(\kappa^1O\text{-}NHC^R)]^{2-}$ isomers are less stable than those with the $\kappa^1$C-coordination of carbene (see Table S2). Topological quantities for Ag–O BCP found in $[Ag(\kappa^1O\text{-}NHC^R)]^{2-}$ isomers are also shown in Table S2 and support the preference of $\kappa^1$C-coordination. Due to its larger size, the $^i$Pr ligand exhibits the possibility of additional interactions involving more than one atom simultaneously.

The inclusion of a second silver atom was considered and optimized structures of $[Ag_2(NHC^R)]^{2-}$ were calculated (Fig. 4). The interaction of the SOMO of $[Ag(NHC^R)]^{2-}$ with the s orbital of the second silver atom constitutes the Ag–Ag bond, which is the HOMO−4 of the compounds with R = H (Fig. 4) and R = Me or the HOMO for R = $^i$Pr. The Ag–C bond, found in HOMO−8 for R = H (Fig. S12) and R = Me or the HOMO−7 for R = $^i$Pr, shows distances shorter than those of the $[Ag(NHC^R)]^{2-}$ compounds (Table S3) with higher values for BDEs (Table S1). The formation of the Ag–Ag bond and the reinforcement of the Ag–C bond suggest that this could be the first step in the mechanism of NP formation. In fact, the reaction of the addition of a silver atom to $[Ag(NHC^R)]^{2-}$ is an exergonic process (for example, −53.7 kcal mol$^{-1}$ for R = Me).

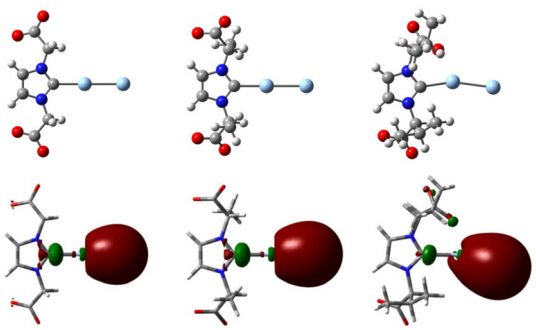

**Fig. 4** Optimized structures of $[Ag_2(NHC^R)]^{2-}$ for R = H, Me and $^i$Pr (top) and HOMO−4 for R = H and Me and HOMO for R = $^i$Pr (bottom).

The topological properties of the compounds $[Ag_2(NHC^R)]^{2-}$ are summarized in Table 3. For the sake of comparison, the simplest $Ag_2$ cluster is also included. This shows a Ag–Ag bond length of 2.575 Å, which is only ∼0.04 Å longer than the experimental distance.[44] The analysis of Table 3 reveals changes upon coordination. The Ag–Ag bond is weaker in the complexes $[Ag_2(NHC^R)]^{2-}$, as evidenced by lower values of both the electron density $\rho(r)$ and its Laplacian at the Ag–Ag BCP relative to the $Ag_2$ dimer. This is consistent with the observed elongation of the Ag–Ag distance and the decrease in the Ag–Ag bond energetic parameters per electron listed in Table 3. In contrast, a strengthening of the Ag–C bond is clearly established when comparing Ag–C data (Table 2) with the $Ag_2$–C complexes (Table 3). According to Bianchi's classification,[37] the $\lvert V_{BCP}\rvert/G_{BCP}$ ratio at Ag–C BCPs suggests an intermediate bond regime, lying between ionic and covalent. The low electron density values, positive Laplacian values and small negative energy densities per electron support the classification of this interaction as a dative bond with strong ionic character. This notion of a weak covalence component is reinforced by the values of the delocalization index $\delta$(Ag,C) and the $\lvert H_{BCP}\rvert/\rho_{BCP}$ ratio, aligning with findings from previous studies on silver precursor complexes.[45,46] For the Ag–Ag interaction, the $\lvert V_{BCP}\rvert/G_{BCP}$ ratio, though its smaller magnitude compared to the Ag–C bonds suggests a slightly lower degree of covalence; nonetheless, the QTAIM descriptors remain consistent with typical metallic bonding characteristics.[45–48] Finally, the bulkier nature of the $^i$Pr substituent facilitates simultaneous interactions between the silver atom and several ligand atoms, resulting in a two-fold interaction mechanism: the C and O interactions maintain the aforementioned covalent character, while the Ag–H interaction is classified as a van der Waals (vdW) type, supported by the $\lvert V_{BCP}\rvert/G_{BCP}$ ratio being lower than 1 and the positive value of the $H_{BCP}/\rho_{BCP}$ ratio at its BCP.

The subsequent growth of nanoparticles through the addition of silver atoms was examined for the simplest case, R = H. The structures of $[Ag_n(NHC^H)]^{2-}$ (for $n$ = 3 and 4) were optimized, yielding two possible arrangements of silver atoms for $n$ = 3 (Fig. S13). Selected structural and topological para-

**Table 3** Selected local and integrated topological properties of the electron density at the Ag–X (X being Ag, C, O and H) for $Ag_2$ cluster and $[Ag_2(NHC^R)]^{2-}$ complexes[a]

| Complex | Ag–X | $Dist_{(Ag-X)}$ | $\rho$ | $V^{2\Im}$ | $\delta(A\gamma,X)$ | $\int_{Ag\cap X}\rho$ | $\lvert V\rvert/G$ | $H/\rho$ | $E_{int}$ |
|---|---|---|---|---|---|---|---|---|---|
| $Ag_2$ | Ag | 2.575 | 0.052 | 0.141 | 1.288 | 0.597 | 1.242 | −0.217 | −12.268 |
| $[Ag_2(NHC^H)]^{2-}$ | Ag | 2.651 | 0.046 | 0.102 | 0.919 | 0.553 | 1.285 | −0.22 | −14.32 |
| | C | 2.108 | 0.102 | 0.274 | 0.804 | 0.878 | 1.308 | −0.299 | −40.632 |
| $[Ag_2(NHC^{Me})]^{2-}$ | Ag | 2.649 | 0.046 | 0.102 | 0.919 | 0.554 | 1.286 | −0.221 | −14.32 |
| | C | 2.108 | 0.102 | 0.274 | 0.795 | 0.913 | 1.308 | −0.299 | −40.632 |
| $[Ag_2(NHC^{iPr})]^{2-}$ | Ag | 2.664 | 0.045 | 0.101 | 0.883 | 0.551 | 1.276 | −0.216 | −14.067 |
| | C | 2.131 | 0.096 | 0.281 | 0.731 | 0.785 | 1.277 | −0.278 | −38.649 |
| | O | 2.279 | 0.02 | 0.068 | 0.18 | 0.198 | 1 | 0 | −5.188 |
| | H | 2.516 | 0.016 | 0.042 | 0.08 | 0.137 | 0.957 | 0.028 | −3.067 |
| | H | 3.076 | 0.007 | 0.017 | 0.036 | 0.072 | 0.838 | 0.089 | −1.015 |

[a] For units and definitions, see the footnote of Table 2.

meters are summarized in Table S4. Both reactions are exergonic, supporting the proposed pathway for nanoparticle growth, with the corresponding energy profile depicted in Fig. S14. The topological and local properties of the complexes $[Ag_n(NHC^H)]^{2-}$ (for $n$ = 3 and 4) were analyzed relative to their parent $Ag_n$ clusters (see Table S3 in SI). Specifically, for the $n$ = 4 system, we restricted our analysis to the open structure of Ag. This selection ensures consistency, as this geometry closely matches the optimized configuration of the $[Ag_4(NHC^H)]^{2-}$ species. A critical finding across all studied complexes ($n$ = 3 and 4) were the exclusive presence of Ag–C BCPs, confirming that the smaller H substituent prevents the simultaneous interaction of the Ag atom with multiple ligand atoms. A clear trend related to cluster size was observed: Ag–C distances decreased compared to smaller $n$ = 1 and 2 clusters, indicating a stronger coordination bond. In contrast, the Ag–Ag distances increased relative to their respective pristine $Ag_n$ clusters, suggesting a destabilization or elongation of the core metallic bonds upon carbene coordination. Despite these geometric changes, the fundamental QTAIM descriptors for both the Ag–Ag and Ag–C interactions maintained the characteristic features (*e.g.* the intermediate bond regime for Ag–C previously established for the smaller).

The coordination of $(NHC^R)^{2-}$ ligands to a silver cluster containing 20 atoms was then investigated. The optimized $T_d$-symmetric structure of the $Ag_{20}$ cluster, reported by Dixon,[49] was used as the ligand coordination platform. Three different types of coordination sites were considered: face (F), vertex (V), and edge (E). The optimized structures of $[Ag_{20}(NHC^H)]^{2-}$ for these three scenarios are presented in Fig. 5, while the corresponding optimized structures for $[Ag_{20}(NHC^{Me})]^{2-}$ and $[Ag_{20}(NHC^{iPr})]^{2-}$ are shown in Fig. S15 and S16, respectively. As the nanoparticle size increases, the ligand interaction invariably involves multiple Ag atoms. Differences in the relative $\Delta G$ energies among the three coordination modes are collected in Table S4 indicating that the preferred coordination site depends on the R substituent. Specifically, edge coordination is favoured for R = Me and $^i$Pr, while vertex coordination is only preferred for R = H. The overall stability of the carbene-nanoparticle complex is not determined solely by the primary

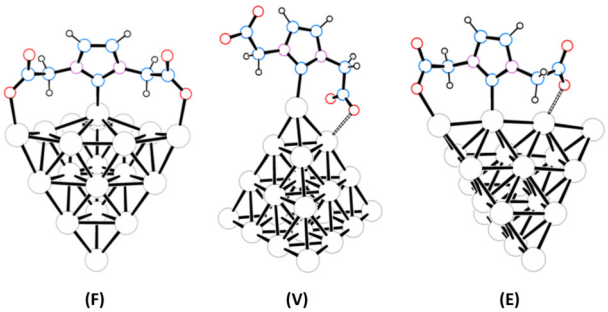


**Fig. 5** Optimized structures of $[Ag_{20}(NHC^H)]^{2-}$ with the carbene ligand coordinated to a silver atom located on the face (F), vertex (V) and edge (E).

Ag–C interaction but is also significantly influenced by the maximization of secondary Ag–O and Ag–H ones. As the nanoparticle size increases, these secondary interactions become progressively more important. The carboxylate groups, and to a lesser extent the methyl groups, begin to play a substantial role by coordinating to adjacent silver atoms. The resulting Ag–O and Ag–H bond distances fall within the ranges of 2.20–2.55 Å and 2.29–3.52 Å, respectively (Tables 4 and S5). The robust nature of the Ag–carboxylate interaction provides considerable stabilization, reinforcing the preferred coordination geometry. In fact, the optimization of the possible vertex complex for R = $^i$Pr yields an isomer of edge complex where the interactions of carboxylate are maximized. Selected QTAIM calculations for $[Ag_{20}NHC^H]^{2-}$ clusters are presented in Table 4 (with values for Me and $^i$Pr in Table S5). The total stability of the different conformers shown in Table S4 is fully consistent with the sum of interaction energy contributions ($\sum E_{int}$) for the Ag–X (X = C, O, H) bonds, as estimated using Espinosa's energy term (Tables 4 and S5). This agreement emphasizes the necessity of considering all possible stabilizing interactions between the carbene and the Ag cluster for a proper description. The $|V_{BCP}|/G_{BCP}$ ratio of the Ag–Ag bonds generally ranges from 1.187 to 1.303. These values are typically smaller than, or comparable to, those of Ag–C bonds, but

**Table 4** Selected local and integrated topological properties of the electron density at the Ag–X (X being C, O and H) for $[Ag_{20}(NHC^{H})]^{2-}$ complexes[a]

| Complex | X | $Dist_{(Ag-X)}$ | $\rho$ | $V^{2\,3}$ | $\delta(A\gamma,X)$ | $\lvert V\rvert/G$ | $H/\rho$ | $E_{int}$ |
|---|---|---|---|---|---|---|---|---|
| $[Ag_{20}(NHC^{H})]^{2-}$ (F) | C | 2.212 | 0.083 | 0.231 | 0.648 | 1.25 | −0.233 | −30.107 |
| | O | 2.25 | 0.059 | 0.263 | 0.449 | 1.08 | −0.097 | −24.148 |
| | O | 2.25 | 0.059 | 0.263 | 0.449 | 1.08 | −0.097 | −24.148 |
| | H | 2.499 | 0.016 | 0.04 | 0.076 | 0.962 | 0.022 | −2.823 |
| | H | 2.499 | 0.016 | 0.04 | 0.076 | 0.962 | 0.022 | −2.823 |
| $[Ag_{20}(NHC^{H})]^{2-}$ (V) | C | 2.145 | 0.095 | 0.264 | 0.724 | 1.282 | −0.274 | −37.007 |
| | O | 2.482 | 0.038 | 0.141 | 0.275 | 1.084 | −0.086 | −13.172 |
| | O | 2.533 | 0.034 | 0.125 | 0.249 | 1.076 | −0.076 | −11.604 |
| | C | 2.987 | 0.015 | 0.046 | 0.038 | 0.942 | 0.042 | −3.136 |
| $[Ag_{20}(NHC^{H})]^{2-}$ (E) | C | 2.172 | 0.089 | 0.261 | 0.673 | 1.257 | 0.253 | −34.498 |
| | O | 2.313 | 0.052 | 0.222 | 0.391 | 1.08 | −0.092 | −20.385 |
| | O | 2.222 | 0.064 | 0.286 | 0.472 | 1.089 | −0.11 | −26.657 |
| | H | 2.644 | 0.014 | 0.041 | 0.051 | 0.927 | 0.051 | −2.823 |
| | H | 2.719 | 0.012 | 0.033 | 0.041 | 0.912 | 0.058 | −2.195 |

[a] For units and definitions see the footnote of Table 2.

notably higher than those found for Ag–O BCPs. This hierarchical relationship suggests a stronger covalent character for the Ag–Ag and Ag–C interactions compared to the Ag–O interaction, where the $|V_{BCP}|/G_{BCP}$ ratio close to 1 indicates a significantly less covalent, or predominantly electrostatic, character. Moreover, analysis of the topological and local properties confirms that Ag–Ag interactions within the cluster are consistent with weakly covalent argentophilic bonds previously reported for similar compounds.[45,46,48,50,51] Finally, there is a direct correlation between the size of the R substituent and the number of possible Ag–carbene interactions. The fact that the interaction strength of Ag–C, Ag–O, and Ag–H bonds appears to be of the same order of magnitude across the series (Tables 4 and S5) confirms the crucial role of these additional Ag–O and Ag–H interactions.

From the experimental results described above, it can be inferred that each carbene ligand is associated with approximately 30 silver atoms. To further investigate this, nanoparticles composed of 30 silver atoms and a single NHC ligand, $[Ag_{30}(NHC^{R})]^{2-}$ (R = H, Me, iPr), were analyzed. The $Ag_{30}$ cluster structure reported by Dixon[49] was used as a model, and the corresponding optimized $[Ag_{30}(NHC^{R})]^{2-}$ nanoparticles are shown in Fig. 6. This model provides a satisfactory description of NP, as evidenced by the comparison of the experimental IR spectrum with the calculated spectrum for $[Ag_{30}(NHC^{H})]^{2-}$ (Fig. 7). In particular, the antisymmetric vibrations of the two carboxylate groups observed at 1627 and 1571 $cm^{-1}$ are well reproduced by the calculated absorptions at 1666 and 1582 $cm^{-1}$. The first band is attributed to the $\kappa^1$-O coordinated carboxylate group, while the second is assigned to the second carboxylate group that exhibits $\kappa^1$-O,$\kappa^1$-O′bidentate coordination.

The comprehensive QTAIM results for the $[Ag_{30}(NHC^{R})]^{2-}$ clusters are presented in Table S6 (SI). Our findings for these large clusters confirm a critical requirement for accurate modelling: the mandatory consideration of all possible interactions between the ligand and the silver nanoparticle is essential for a proper understanding of the binding mechanism. Throughout the series, from the smallest clusters $n$ = 1 to $n$ = 30, the overall stability of the complexes increases consistently with the size of the nanoparticle. As a rule, the stability depends on the nature of the R substituent, following the consistent trend: H > Me > $^{i}$Pr. This ranking suggests that, while bulkier ligands (such as $^{i}$Pr) facilitate a greater number of sim-

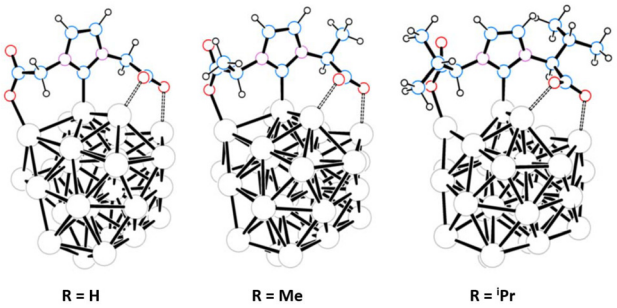


**Fig. 6** Optimized structures of NP models $[Ag_{30}(NHC^{R})]^{2-}$.

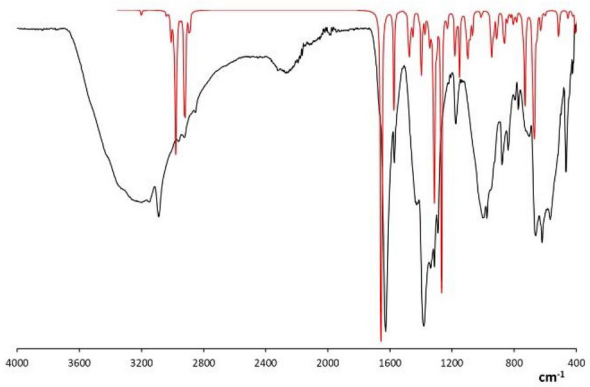


**Fig. 7** Comparison between the experimental IR spectra of Ag($NHC^{H}$)-NPs (**3a**, black) and the calculated for the model $[Ag_{30}(NHC^{H})]^{2-}$ (red).

ultaneous secondary interactions (*e.g.*, Ag–H or Ag–O), the overall most stable coordination is achieved with the less sterically demanding ligand with R = H. In fact, the highest values of BDEs for the Ag–C bond are found in $[Ag_n(NHC^H)]^{2-}$ compounds (see Fig. S17).

# Experimental

### General considerations

All preparations and other operations were carried out under anaerobic conditions. For all solutions or reactions conducted in aqueous media, ultrapure water (Millipore) was used from a Milli-Q water purification system (model Vent Filter MPK01). Chemicals were obtained from various commercial sources and used as supplied. UV-Vis analyses were performed using a Jasco V-730 spectrophotometer, with measurements taken at room temperature and at a concentration of $10^{-3}$ M. Infrared spectra were recorded using the ATR technique on a PerkinElmer FT-IR Spectrum Two (Waltham, MA, USA). NMR spectra were recorded at the Centro de Investigaciones, Tecnología e Innovación (CITIUS) of the University of Sevilla using Avance III spectrometers (Billerica, MA, USA). $^1$H and $^{13}C\{^1H\}$ NMR shifts were referenced to residual signals from deuterated solvents. All data are reported in ppm downfield from $Si(CH_3)_4$. Polarimetry was carried out using a JASCO P-2000 digital polarimeter (JASCO Analitica Spain s.l., Madrid) and the measurements were carried out at room temperature. Elemental analyses (C, H, N) were performed by CITIUS of the University of Sevilla on an Elemental LECO CHNS 93 analyzer (LECO Corporation, St Joseph, MI, USA).

### Synthesis of silver carbene complexes, $Na_3[Ag(NHC^R)_2]$ (2a–d)

NHC-dicarboxylate silver complexes $Na_3[Ag(NHC^R)_2]$ (R = H **2a**; Me, **2b**; $^i$Pr, **2c**; and $^i$Bu, **2d**) were synthesized following established procedures.[15,16] Imidazolium dicarboxylate $HIm^R$ (**1a–d**), (2 mmol) were reacted with $Ag_2O$ (0.5 mmol, 116 mg) in a Schlenk tube. The solids, which were NMR identified as the actual $Na_3[Ag(NHC^R)_2]$ complexes, were dried under vacuum for 5 minutes and suspended in 10 mL of deoxygenated Millipore water. NaOH (3 mmol, 120 mg) was then added, and the reaction mixture was stirred at room temperature for 18 hours. After completion, the mixture was centrifuged and filtered. The resulting clear solution was stored in a sealed ampoule as a stock solution, with an assumed silver complex concentration of 0.1 M.

### Synthesis of NHC-stabilized silver nanoparticles $Ag(NHC^R)$-NPs (3a–d)

The stability of $Ag(NHC^R)$-NPs was strongly influenced by both the nature and the concentration of the silver–carbene precursor complex $Na_3[Ag(NHC^R)_2]$ (**2a–d**). As a representative example, $Ag(NHC^H)$-NPs (**3a**) were synthesized using a 1 mM solution of $Na_3[Ag(NHC^H)_2]$ (**2a**), prepared by diluting 100 μL of the 0.1 M stock solution in 9.9 mL of deoxygenated water. Under a nitrogen atmosphere, this solution (10 mL) was added dropwise *via* a pressure-equalizing funnel to a freshly prepared $NaBH_4$ solution (2 equivalents, 30 mL, 2 mM) in deoxygenated Millipore water. The initial colorless mixture turned yellow, indicating nanoparticle formation. To obtain nanoparticles at higher concentrations, the amount of silver precursor can be adjusted accordingly (*e.g.* 400 μL of the 0.1 M stock solution in 9.6 mL of water yields a 4 mM solution).

### Isolation and characterization of silver nanoparticles 3a

The solid form of nanoparticles **3a** was obtained from a freshly prepared 4 mM colloidal dispersion. Silver nanoparticles were isolated using ultracentrifugation followed by lyophilization. Samples were centrifuged with a Beckman Coulter Optima MAX ultracentrifuge at 55 000 rpm ($1.15 \times 10^5 g$) for 1 hour at 4 °C. Subsequently, water was removed by freeze-drying. Samples were frozen at −85 °C under high vacuum overnight using a Telstar Lyoquest −85 °C Plus lyophilizer, yielding a dry silver nanoparticle powder. Solid nanoparticle **3a** was characterized by ATR-IR spectroscopy and elemental analysis. IR (ATR, $cm^{-1}$): 3201 (br), 3090 (s), 2961 (w), 2922 (w), 2865 (w), 2271 (w), 1627 (vs), 1571 (m), 1426 (m), 1381 (vs), 1313 (s), 1291 (s), 1176 (m), 1000 (s), 975 (s), 878 (m), 838 (m), 795 (w), 773 (w), 706 (w), 660 (s), 619 (s), 564 (s), 465 (m), 423 (w). Elemental anal. calc. for $C_7H_{16}Ag_{30}N_2Na_2O_9$ (**3a**): C, 2.37; H, 0.45; N, 0.79. Found: C, 1.94; H, 0.42, N, 1.48%.

### Structural characterization of silver nanoparticles

Structural characterization was performed using Dynamic Light Scattering (DLS) and Transmission Electron Microscopy (TEM). DLS measurements, carried out with a Zetasizer Nano ZSP, determined the hydrodynamic size distribution of nanoparticles in colloidal suspension by analyzing laser-induced light scattering. TEM analysis, conducted with a Talos X200 microscope operating at 200 kV and 5 nA, provided insight into nanoparticle morphology. TEM images were processed using ImageJ software (version 1.43, NIH) to obtain more detailed size information.[52]

### Catalytic reduction of 4-nitrophenol using AgNPs 3a

The catalytic reduction of 4-nitrophenol (4-NP) was carried out in a quartz cuvette using freshly prepared stock solutions. Solution 1 consisted of 4-NP (7.5 mg, 36 μmol) and $NaBH_4$ (10 equiv., 14 mg, 360 μmol) dissolved in Millipore $H_2O$ to a final volume of 500 mL. Solution 2 contained the catalyst precursor $Na_3[Ag(NHCH)_2]$ (**2a**, 1 mmol) dissolved in 10 mL of Millipore $H_2O$. An aliquot of 100 μL of solution 2 was diluted in 3 mL of Millipore $H_2O$, and 5 μL of this diluted solution was added to 10 mL of solution 1. The reaction progress was monitored by UV-visible spectroscopy at one-minute intervals.

### Catalytic $NaBH_4$ hydrolysis to $H_2$ using AgNPs 3a

The catalytic hydrolysis of $NaBH_4$ was conducted in a closed system using a round-bottom flask equipped with a magnetic stirring bar under continuous agitation. In a typical experiment, 10 mL of an aqueous solution containing the catalyst precursor $Na_3[Ag(NHC^H)_2]$ (**2a**, 0.05 mmol) was added to

10 mL of a freshly prepared $NaBH_4$ solution (1 mmol, 38.6 mg), generating AgNPs **3a** *in situ* upon contact with the reducing agent. The evolved $H_2$ was collected by water displacement in an inverted 100 mL graduated burette submerged in a water-filled crystallizer, with gas volume measured as a function of time to monitor reaction kinetics at room temperature.

### Computational details

The electronic structure and geometries of the silver–carbene complexes $[Ag(NHC^R)]^{2-}$, $[Ag(NHC^R)]^-$, $[Ag_2(NHC^R)]^{2-}$, $[Ag_n(NHC^H)]^{2-}$ ($n$ = 3, and 4) and $[Ag_n(NHC^R)]^{2-}$ (R = H, Me and $^i$Pr with $n$ = 20 and 30) were investigated using density functional theory at the PBE-D3/def2TZVP level of calculation using Gaussian16.[53] Clusters $Ag_2$, $Ag_3$, and $Ag_4$ were also optimized for an appropriate comparison. This level of calculation was previously used for its ability to reproduce geometries in good agreement with the periodic DFT calculations in a few calibration studies.[45,46] The initial coordinates for clusters $Ag_n$ for $n$ = 20 and 30 were taken from the optimized coordinates reported by Dixon and coworkers.[49] Bond dissociation energies (BDEs) were calculated as the difference in the total electronic energies of the optimized fragments. Frequency calculations were carried out at the same level of theory to identify all stationary points as minima (zero imaginary frequencies). The theoretical IR spectra were scaled by a factor of 0.96.[54,55] Topology parameters were studied within the framework of the QTAIM method implemented in AIMALL program.[56] Coordinates of optimized compounds are collected in the SI (Table S7).

## Conclusions

The stabilization of silver nanoparticles by amino acid-derived N-heterocyclic carbenes was demonstrated by the preparation and study of $Ag(NHC^R)$-NPs (R = H **3a**; Me, **3b**; $^i$Pr, **3c**; and $^i$Bu, **3d**). The aqueous solution concentration and the nature of the R substituent was found to control the stability of AgNP solutions. In fact, **3a** (R = H) exhibits remarkable stability in water and can be isolated by ultracentrifugation and lyophilization. Remarkably, a stable AgNP solution was obtained by redissolution in water of solid **3a**. Nanoparticles **3a** behave as an active and versatile nanocatalyst in aqueous media, promoting both the model reduction of 4-nitrophenol to 4-aminophenol and the catalytic hydrolysis of $NaBH_4$ to generate $H_2$ under basic conditions. These complementary reactivity profiles place **3a** among related NHC–AgNP systems for benchmark transformations,[22] highlighting its mediation of electron and hydride transfer processes at the metal–solution interface. Overall, this dual functionality identifies **3a** as a promising platform for environmentally oriented catalysis, particularly for nitroaromatic remediation coupled with on-demand hydrogen generation from $NaBH_4$ in water. The nucleation and growth of the $Ag(NHC^R)$-NPs was modeled using DFT, while QTAIM was used to analyze the bonding characteristics of the Ag–Ag and Ag–C (carbene) interactions. Noteworthy, the bond dissociation energy of the Ag–C(carbene) bond decreases with increasing steric bulk of R, consistent with the experimental observations. The study deals with relatively small nanoparticle size (only up to 30 Ag atoms), which can be considered far from having bulk behaviour. However, the $[Ag_{30}(NHC^H)]^{2-}$ model that corresponds to **3a**, selected to account for the experimental Ag : NHC ratio of 30 : 1, provides a satisfactory match with the experimental IR spectrum. The QTAIM results will be sensitive to the nanoparticle's specific geometry and the coordination site of the carbene. Nonetheless, projection of these findings to larger nanoparticles suggests that the interaction may not be exclusive to a single Ag–C interaction but rather involve multiple surface Ag–O and Ag–H interactions.

## Author contributions

Conceptualization, F. M., R. A. and A. G.; funding acquisition, A. G.; investigation, C. J. C. and S. G.; methodology, C. J. C., R. A., F. M. and A. G.; resources, F. M., A. G. and R. A.; supervision, F. M.; theoretical studies, R. A. and A. G.; writing – original draft, F. M., R. A., and A. G.; writing – review and editing, C. J. C., F. M., R. A., and A. G. The manuscript was written through contribution of all authors. They have read and agreed to the published version of the manuscript.

## Conflicts of interest

There are no conflicts to declare.

## Data availability

The data supporting this article have been included as part of the supplementary information (SI). Supplementary information: Fig. S1–S17 and Tables S1–S7. See DOI: https://doi.org/10.1039/d6dt00206d.

## Acknowledgements

Financial support from the University of Sevilla through the VI Plan Propio de Investigacion y Transferencia (grant number VIPPIT-2021-I.5). C. J. C. thanks a research contract from PAIDI 2020, supported by the European Social Fund and the Junta de Andalucia. The authors thank the Centro de Investigaciones, Tecnologia e Innovacion (CITIUS) of the University of Sevilla for providing several research services, and Centro de Servicios de Informatica y Redes de Comunicaciones (CSIRC), Universidad de Granada, for providing the computing time.

## References

1 A. Dhaka, S. Chand Mali, S. Sharma and R. Trivedi, *Results Chem.*, 2023, **6**, 101108.

2 L. Song, Y. Wang, M. Yang and Y. Huang, *J. Nanopart. Res.*, 2023, **25**, 255.
3 R. Sharma, *Orient. J. Chem.*, 2020, **36**, 334–338.
4 Y. An, J. Yu and Y. Han, *Chin. J. Chem.*, 2019, **37**, 76–87.
5 A. V. Zhukhovitskiy, M. J. MacLeod and J. A. Johnson, *Chem. Rev.*, 2015, **115**, 11503–11532.
6 M. Ghosh and S. Khan, *ACS Catal.*, 2023, **13**, 9313–9325.
7 C. A. Smith, M. R. Narouz, P. A. Lummis, I. Singh, A. Nazemi, C.-H. Li and C. M. Crudden, *Chem. Rev.*, 2019, **119**, 4986–5056.
8 C. K. Lee, C. S. Vasam, T. W. Huang, H. M. J. Wang, R. Y. Yang, C. S. Lee and I. J. B. Lin, *Organometallics*, 2006, **25**, 3768–3775.
9 I. P. Chebotareva, A. R. Sungatullina, K. V. Pidgirnaya, D. A. Elkina, P. M. Ivantcova and M. P. Nikitin, *Inorg. Chem. Commun.*, 2025, 115033.
10 L. M. Sherman, M. D. Finley, R. K. Borsari, N. Schuster-Little, S. L. Strausser, R. J. Whelan, D. M. Jenkins and J. P. Camden, *ACS Omega*, 2022, **7**, 1444–1451.
11 A. M. Ruiz-Varilla, E. A. Baquero, B. Chaudret, E. de Jesús, C. Gonzalez-Arellano and J. C. Flores, *Catal. Sci. Technol.*, 2020, **10**, 2874–2881.
12 E. A. Baquero, S. Tricard, J. C. Flores, E. de Jesús and B. Chaudret, *Angew. Chem., Int. Ed.*, 2014, **53**, 13220–13224.
13 C. J. Carrasco, F. Montilla, E. Álvarez, A. Galindo, M. Pérez-Aranda, E. Pajuelo and A. Alcudia, *Dalton Trans.*, 2022, **51**, 5061–5071.
14 C. J. Carrasco, F. Montilla, E. Villalobo, M. Angulo, E. Álvarez and A. Galindo, *Molecules*, 2024, **29**, 4608.
15 C. J. Carrasco, F. Montilla, E. Álvarez, J. M. Calderón-Montaño, M. López-Lázaro and A. Galindo, *J. Inorg. Biochem.*, 2022, 111924.
16 C. J. Carrasco, F. Montilla, E. Álvarez, M. d. M. Conejo, A. Pastor and A. Galindo, *Inorg. Chim. Acta*, 2023, **557**, 121717.
17 K. Duanmu and D. G. Truhlar, *J. Phys. Chem. C*, 2015, **119**, 9617–9626.
18 M. L. McKee and A. Samokhvalov, *J. Phys. Chem. A*, 2017, **121**, 5018–5028.
19 T. Tsuneda, *J. Comput. Chem.*, 2019, **40**, 206–211.
20 G. U. Kuda-Singappulige and C. M. Aikens, *J. Phys. Chem. A*, 2021, **125**, 9450–9458.
21 M. Farshad, D. C. Perera and J. C. Rasaiah, *Phys. Chem. Chem. Phys.*, 2021, **23**, 25507–25517.
22 D. T. H. Nguyen, L. R. Shultz, T. Jurca and A. Nazemi, *Langmuir*, 2023, **39**, 3204–3215.
23 P. Vu Nhat, N. T. Si, N. T. Tien and M. T. Nguyen, *J. Phys. Chem. A*, 2021, **125**, 3244–3256.
24 L. Kuster, M. Bélanger-Bouliga, T. E. Shaw, T. Jurca, A. Nazemi and M. Frenette, *Nanoscale*, 2024, **16**, 11052–11068.
25 R. F. W. Bader and H. Essén, *J. Chem. Phys.*, 1984, **80**, 1943–1960.
26 R. F. W. Bader, in *Atoms in molecules: A Quantum Theory*, 1990.
27 R. F. W. Bader, *Chem. Rev.*, 1991, **91**, 893–928.
28 R. F. W. Bader, *Monatsh. Chem.*, 2005, **136**, 819–854.
29 F. Cortés-Guzmán and R. F. W. Bader, *Coord. Chem. Rev.*, 2005, **249**, 633–662.
30 P. L. A. Popelier, *Atoms in Molecules. An Introduction*, Pearson Education, 2000.
31 Y. R. Mejía and N. K. Reddy Bogireddy, *RSC Adv.*, 2022, **12**, 18661–18675.
32 N. Pradhan, A. Pal and T. Pal, *Colloids Surf., A*, 2002, **196**, 247–257.
33 H. N. Abdelhamid, *Int. J. Hydrogen Energy*, 2021, **46**, 726–765.
34 Y. Sun and Y. Xia, *Analyst*, 2003, **128**, 686.
35 M. S. J. Khan, L. Mohd Sidek, T. Kamal, S. B. Khan, H. Basri, M. H. Zawawi and A. N. Ahmed, *J. Environ. Manage.*, 2024, **354**, 120228.
36 M. Abdollahi and A. Mohammadirad, *Encyclopedia of Toxicology*, 3rd edn, 2014, pp. 575–577.
37 G. Gervasio, R. Bianchi and D. Marabello, *Chem. Phys. Lett.*, 2004, **387**, 481–484.
38 P. Macchi, D. M. Proserpio and A. Sironi, *J. Am. Chem. Soc.*, 1998, **120**, 13429–13435.
39 P. Macchi, L. Garlaschelli and A. Sironi, *J. Am. Chem. Soc.*, 2002, **124**, 14173–14184.
40 P. Macchi and A. Sironi, *Coord. Chem. Rev.*, 2003, **238–239**, 383–412.
41 E. Espinosa, I. Alkorta, J. Elguero and E. Molins, *J. Chem. Phys.*, 2002, **117**, 5529–5542.
42 E. Espinosa, E. Molins and C. Lecomte, *Chem. Phys. Lett.*, 1998, **285**, 170–173.
43 E. Espinosa, I. Alkorta, I. Rozas, J. Elguero and E. Molins, *Chem. Phys. Lett.*, 2001, **336**, 457–461.
44 B. Simard, P. A. Hackett, A. M. James and P. R. R. Langridge-Smith, *Chem. Phys. Lett.*, 1991, **186**, 415–422.
45 M. Puyo, E. Lebon, L. Vendier, M. L. Kahn, P. Fau, K. Fajerwerg and C. Lepetit, *Inorg. Chem.*, 2020, **59**, 4328–4339.
46 C. Lacaze-Dufaure, N. Tarrat, C. Lepetit, Y. Bulteau, D. Loffreda, P. Fau, K. Fajerwerg, M. L. Kahn and F. Rabilloud, *Inorg. Chem.*, 2022, **61**, 7274–7285.
47 R. Bianchi, G. Gervasio and D. Marabello, *C. R. Chim.*, 2005, **8**, 1392–1399.
48 C. Lepetit, P. Fau, K. Fajerwerg, M. L. Kahn and B. Silvi, *Coord. Chem. Rev.*, 2017, **345**, 150–181.
49 M. Chen, J. E. Dyer, K. Li and D. A. Dixon, *J. Phys. Chem. A*, 2013, **117**, 8298–8313.
50 A. Ofori, S. Suvanto, S. Jääskeläinen, L. Koskinen, I. O. Koshevoy and P. Hirva, *Cryst. Growth Des.*, 2015, **16**, 255–264.
51 H. Schmidbaur and A. Schier, *Angew. Chem., Int. Ed.*, 2015, **54**, 746–784.
52 C. A. Schneider, W. S. Rasband and K. W. Eliceiri, *Nat. Methods*, 2012, **9**, 671–675.
53 M. J. Frisch, G. W. Trucks, H. B. Schlegel, G. E. Scuseria, M. A. Robb, J. R. Cheeseman, G. Scalmani, V. Barone, G. A. Petersson, H. Nakatsuji, X. Li, M. Caricato, A. Marenich, J. Bloino, B. G. Janesko, R. Gomperts,

B. Mennucci, H. P. Hratchian, J. V. Ortiz, A. F. Izmaylov, J. L. Sonnenberg, D. Williams-Young, F. Ding, F. Lipparini, F. Egidi, J. Goings, B. Peng, A. Petrone, T. Henderson, D. Ranasinghe, V. G. Zakrzewski, J. Gao, N. Rega, G. Zheng, W. Liang, M. Hada, M. Ehara, K. Toyota, R. Fukuda, J. Hasegawa, M. Ishida, T. Nakajima, Y. Honda, O. Kitao, H. Nakai, T. Vreven, K. Throssell, J. A. Montgomery Jr., J. E. Peralta, F. Ogliaro, M. Bearpark, J. J. Heyd, E. Brothers, K. N. Kudin, V. N. Staroverov, T. Keith, R. Kobayashi, J. Normand, K. Raghavachari, A. Rendell, J. C. Burant, S. S. Iyengar, J. Tomasi, M. Cossi, J. M. Millam, M. Klene, C. Adamo, R. Cammi, J. W. Ochterski, R. L. Martin, K. Morokuma, O. Farkas, J. B. Foresman and D. J. Fox, *Gaussian 09, Revision C.01*, Gaussian, Inc., Wallingford CT, 2016.

54 M. W. Wong, *Chem. Phys. Lett.*, 1996, **256**, 391–399.

55 A. P. Scott and L. Radom, *J. Phys. Chem.*, 1996, **100**, 16502–16513.

56 T. A. Keith, *AIMALL, Version 16.05.18*, TK Gristmill Software, Overland Park, 2016.